Automated 120° MMI Based Downconverter Design

Jelmer David Meuleman
University of Twente
Enschede, the Netherlands
j.d.meuleman@student.utwente.nl

BSc thesis supervisors:
W.A.P.M. Hendriks MSc
Prof. Dr. S.M. García Blanco

***Abstract*—In this work the automated numerical design of an 120° MMI-based downconverter is discussed. A program has been made which is able to quickly estimate the output of thousands MMI's based on one simulated Poynting field. A figure of merit has been defined to, after simulation in multiple dimensions, characterise the performance of the estimated MMI outputs and to select the dimensions with the optimal performance. An MMI in Al_3O_2 was autonomously designed and optimised in approximately eight hours. The average phase error after calibration went as low as 0.08° for a noiseless system and stayed below 1° for systems with an SNR above 45 dB.**

***Index Terms*—Downconverter, MMI, Automation, Al2O3**

I. Introduction

Mach Zehnder interferometers (or MZI's) play an very important role in optics. These can be used to determine phase variations between two collimated beams of light, and MZI's have been used in, among others: Sensors [1], wavemeters [2], modulators [3], and quantum computing [4]. MZI's are typically made with "two inputs-two outputs" (or 2x2) optical couplers [5]. This last elements however poses a problem as it is impossible to directly characterise the aforementioned phase variation. Figure 2b shows the phasor diagram of the output of a 2x2 coupler. An alternative option is shown in [6] in the form of a 3x3 coupler, specifically a 3x3 MMI (or multi mode interferometer) based downconverter. By using a coupler with three output ports, evenly spaced with a 120° phase shift at the outputs, it becomes possible to uniquely define the output, see figure 2a.

A disadvantage, however, is that the design of such 3x3 MMI's is typically numerically determined and that it is very dependent on the specifications of the system in which it is to be integrated. To make the use of these 3x3 MMI more accessible for any system, we created a program that can simulate and optimise a wide range of MMI's and we introduced a novel figure of merit to estimate the performance of these MMI's. First, this figure of merit is defined in section II, followed by the theory of taking measurements and doing calibrations in section III. Then a small section about the Poynting field approximation and section V in which a method is presented to optimise an MMI given a certain MMI width. In section VI the performance of an optimal MMI, designed for use in Al2O3, is evaluated by varFDTD simulations including the addition of noise to simulate a lab environment.

The general design of the proposed downconverter can be seen in figure 1. Please note that, although the design shows a 3x3 MMI, the middle input (left in figure 1) is not connected. Figure 12 shows an example of the typical behaviour of a 3x3 MMI for different input phase differences. Finally, a flow diagram of and a link to the full program made in this report can be found in appendix VII-B.

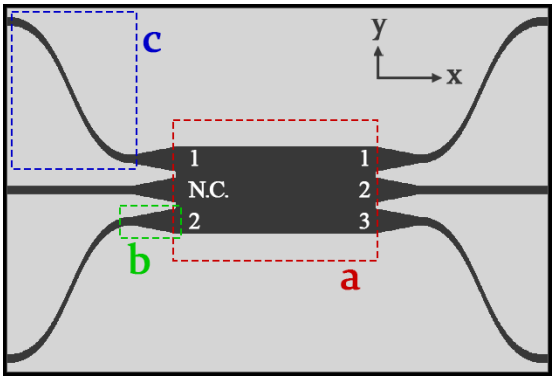

Fig. 1: The general design of the downconverter, with inputs to the left and output to the right. a) MMI body, b) Taper, c) S-bend

II. Figure of Merit

The figure of merit used to evaluate the performance of the MMI's is essentially the summed difference of the ideal and simulated output phasors, see figure 2a. Mathematically, it is defined as follows:

$$FoM = \log_{10}(\frac{1}{3} \cdot \sum_i \Delta\text{phasor}_i) \tag{1}$$

With:

$$\Delta\text{phasor}_i = |\frac{2}{3} \cdot e^{-j(\frac{2\pi}{3} \cdot (i-1))} - P_i(\phi_i) \cdot e^{-j(\phi_i - \phi_1)}| \tag{2}$$

Where P_i and ϕ_i are the amplitude and phase shifts of the sinusoidal output signal of the three output ports and P_{in} is

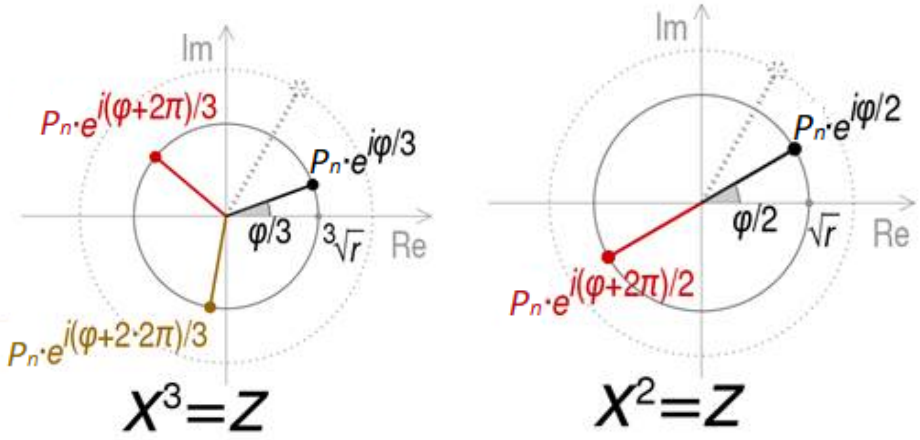

(a) 120° (3x3) MMI output phasors (b) 180° (2x2) MMI output phasors

Fig. 2: Comparison of 120° and 180° spaced phasors

the total power of the input signals. Please note that $(\phi_i - \phi_1)$ is used instead of ϕ_i as this means that only the relative phase shift is evaluated.

The parameters A_i and ϕ_i as used in equation 2 are determined as follows:

$$c_i = \frac{P_i(0) + P_i(\frac{2\pi}{3}) + P_i(\frac{4\pi}{3})}{3} \tag{3}$$

$$e^{j\phi_i} = \frac{\sqrt{\Delta P_i - e^{j\frac{2\pi}{3}}}}{\sqrt{e^{-j\frac{2\pi}{3}} - \Delta P_i}} \tag{4}$$

$$\phi_i = \arg(e^{j\phi_i}) \tag{5}$$

$$A_i = \frac{(P_i(0) - c_i)}{\cos(\phi_i)} \tag{6}$$

With $\Delta P_i = \frac{P_i(\frac{2\pi}{3}) - c_i}{P_i(0) - c_i}$ and such that $A_i > 0$. Derivations for the above equations can be found in appendix VII-C through VII-E. $P_i(\theta)$ denotes the measured output power at port i and the input phase difference θ and is defined as follows:

$$P_i(\theta) = A_i \cos(\theta - \phi_i) + c_i \tag{7}$$

At least three data points, with differing input phase differences, are required to reconstruct the full output of an MMI, as can be seen in the above equations. Those data points are chosen specifically as $P_i(\theta)$ for $\theta = 0, \frac{2\pi}{3}, \frac{4\pi}{3}$. Consequently, three simulations must be run per MMI.

Finally, to make the figure of merit more accurately represent the performance of an MMI that is actually fabricated, a normal distribution with standard deviation σ can be used to average the FoM around every point. This, assuming any deviations in the production process take the shape of a normal distribution, characterises the average performance of the resulting MMI.

III. Measurements and Calibration

The output powers also need to be interpreted as an input phase difference θ. This can be done by constructing the in-phase (I) and quadrature (Q) components from those output powers and then computing the complex signal $s = I + Q \cdot j$. From this we can determine θ using the equations below [7]:

$$I = P_2 - 0.5P_1 - 0.5P_3 \tag{8}$$

$$Q = \frac{\sqrt{3}}{2} \cdot (0.5P_1 - 0.5P_3) \tag{9}$$

$$\theta = \arg(s) \tag{10}$$

Assuming an ideal design and fabrication, those outputs will follow equation 7 with $P_i(\phi_i) = \frac{2}{3}$ and $\phi_i = 0, \frac{2\pi}{3}, \frac{4\pi}{3}$. If that is the case, then $s = \frac{1}{2j}e^{(-i\theta)}$, as shown in [8], which is a circle centered around the origin in the complex plane. Unfortunately, an actually fabricated MMI can deviate from the ideal, either by non-uniformly distributing the input power over the ports, by deviating from the relative 120° phase shift and/or by losses in the MMI. These deviation can be seen as either a rotation, shift and/or partial scaling of the circle s, see figure 3, taken from [7].

These deformation, here called $\hat{s}$, and the resulting errors in the reconstruction of θ can be compensated by blind calibration, assuming enough measurements have been done. The $\hat{s}$ reconstructed from the measured data points is fitted to an ellipse and mathematically re-transformed to a circle after which the transformation parameters become the calibration parameters. The more measurements are done, the better the fit of $\hat{s}$ and the more accurate the calibration process. Any data points with a known reference, i.e., with a known θ, can be used to improve the above mentioned calibration by shifting the resulting angle

after calibration, using least-squares optimisation between the reconstructed $\hat{\theta}$'s and the known θ's. This can resolve any constant phase errors that can remain after calibration due to inaccuracies in the fit of $\hat{s}$.

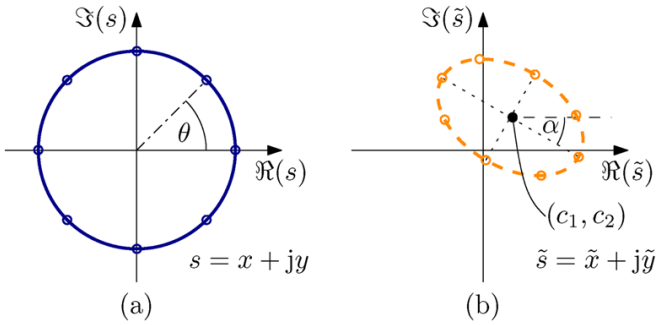

Fig. 3: Unit circle vs ellipse [7]

IV. Poynting field estimation

We used the characteristic that, for any MMI width, the interference pattern in the MMI is a function of the propagation length independent on the location of the MMI end. Using this we can find the interference pattern of a given length MMI by only simulating the longest MMI of interest. Figure 4 shows a comparison between the Poynting fields within a larger and shorter MMI. Notice how the Poynting field in figure 4b is identical to the Poynting field before the dotted line in figure 4a. Please note that the MMI "length" is parallel the propagation direction (x-direction in figure 1) and the MMI "width" is transverse to the propagation direction (y-direction in figure 1).

By integrating the Poynting field at the location and width of the taper interface, we can estimate the output power of the MMI. This is an estimation as the integration yields the power that enters the taper, and not necessarily the output power. Now, by doing this integration for every point along the x-axis of a long MMI we can estimate the output power of many shorter MMI's in the simulation time of only one. The normalised output power for port *i* becomes:

$$Pi = \frac{\int_{T_i} \vec{S_x} dh}{P_{in}} \tag{11}$$

Where $\int_{T_i}$ is the integral over the output taper with $i = 1, 2, 3$ for the three output ports and P_{in} the total input power. Using this method can speed up the simulations by a significant factor approximately equal to the number of desired MMI lengths per MMI width, which can easily range in the thousands.

V. Design

The general design of the proposed downconverter can be seen in figure 1. It consists of three separate subcomponents, which will be discussed here. All sub-components are assumed to be of the same substrate material and height. The first is the MMI body, seen as element (a) in figure 1. It is the region in which the interference patterns are created that determine the behaviour of the MMI. We chose to the shape to be a rectangular cuboid with symmetric port locations, but it can be any shape that allows for the wanted interference patterns [9].

The second subcomponent is the taper, seen as element (b) in figure 1. These can be used to maximise the energy transfer between the waveguides/s-bends and the MMI body, by matching the mode fields at the interface. Essentially tapers are waveguides with slowly increasing or decreasing width [10]. The width and location of the taper on the MMI side are determined by optimising the power overlap between the fundamental TE mode in the taper with the TE_3 mode in the MMI. This is done in simulation, for which the Lumerical FDE solver is used. The efficiency of the taper itself depends on the length and shape of the taper. The taper shape is set by a variable m such that the shape is proportional to the taper length (in the x-direction) to the power m. See figure 5 for examples of the aforementioned shapes [11]. This variable m and the taper length are determined by sweeping over both and choosing the combination that results in the shortest taper with an efficiency equal to or greater than a user defined value.

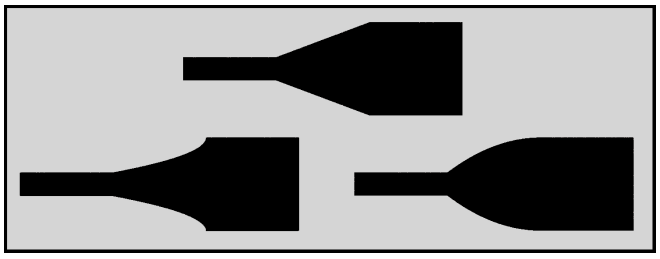

Fig. 5: Three taper shapes. Left to right: $m = 0.5$, $m = 1$ and $m = 2$

The third subcomponent is the S-bend. This is implemented to prevent crosstalk between evanescent waveguides. In general, the shallower the bend, the better the energy transfer [10]. The program determines the shortest length for which the S-bend can create the wanted height difference without a bend radius smaller than the minimum bend radius of the waveguide. It does so using the equation below:

$$L = \sqrt{|\Delta H^2 - 4 \cdot R \cdot \Delta H|} \tag{12}$$

With L the length (x-axis) and ΔH the increase in height (y-axis) of the S-bend and R the minimum bend radius of the waveguides [12].

VI. Results

The following subsection shows the successful simulation of an MMI. The program has been run using the input parameters in table I. The output MMI validations are created by simulating 180 samples at increasing phase difference

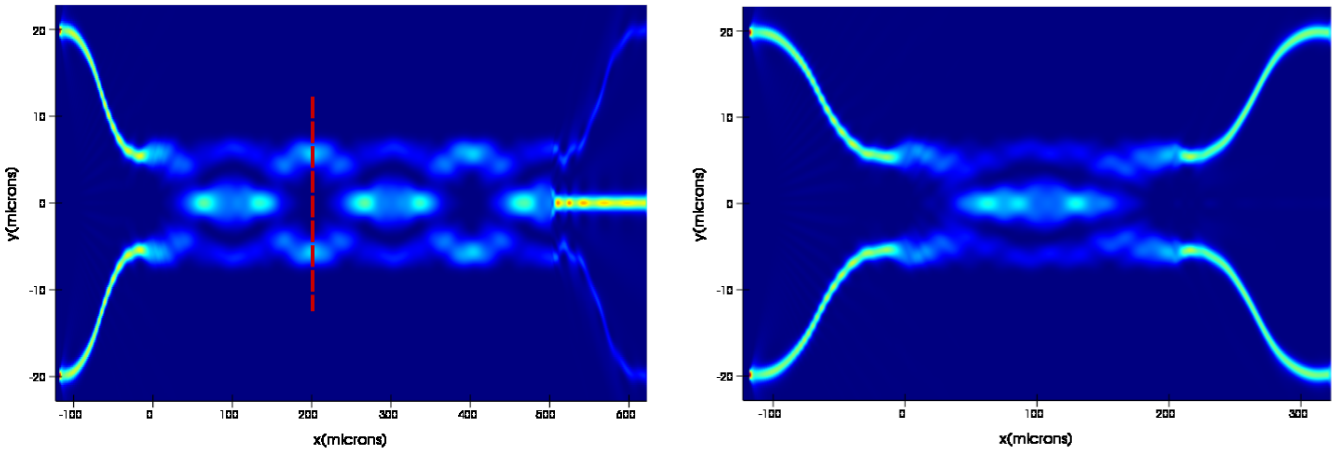

(a) Full-side MMI

(b) Shortened MMI

Fig. 4: Comparison of Poynting fields inside MMI's

between two sources of equal amplitude placed at the inputs, ranging from 0 to 2π radians. These validation simulations were done by varFDTD simulations. Blind calibration test results are determined *without* access to the set of input phase differences, while the relative calibration is done *with* access to full set of input phase differences. These input phase differences were used to remove any remaining constant phase shift after calibration by least squares fitting the reconstructed data with the input data, see section III above. The automation program, which run consisted of 81 MMI width points and 3779 MMI length points took approximately eight hours to complete.

TABLE I

Set parameter	**Value**
Wavelength	1.985 [um]
Waveguide width	1.5 [um]
Minimum waveguide bend radius	300 [um]
Minimum waveguide spacing	19.85 [um]
Substrate height	0.55 [um]
Production σ	0.1 [um]
Substrate material	Al2O3
Cladding material	SiO2 (Palik)

The resulting figure of merit scores, with and without probability distribution, can be seen in figure 9 (please note that some of the figures have been placed in appendix VII-A for better readability). One of the first things the reader might notice is that the FoM results with the probability distribution looks slightly "burrier". Which makes sense as a convolution of an image with a Gaussian is literally a blur filter. This also shows that using the probability distribution can be useful for the elimination of "unstable points", meaning points that might have a good FoM at their exact dimensions, but deteriorate quickly for a little shift in width and/or height of the MMI. See figure 10 for an example. Please note that this last figure is not made using the same system specifications as compared to the rest of the results.

The output dimensions for the MMI with the best FoM (with probability function) are listed in table II. Figure 11a shows the normalized output powers P_i for one period of θ, simulated with varFDTD. One of the first things the reader might notice when comparing these results to 11b, which shows the estimation as reconstructed from the dimension sweep, is that the two do not share the same amplitudes. The maximum powers for the simulated and reconstructed outputs are $0.5451, 0.5225, 0.5268$ and $0.4680, 0.4021, 0.3978$, respectively. It is possible this is due to the inclusion of the tapers, s-bends and output waveguide in the validation simulation (which were omitted in the sweep). The fact that P_1 and P_3, both of which are connected to an s-bend, show a higher difference in amplitude could support the aforementioned theory. The phase shifts relative to P_1 are more similar, being approx. 112° and 238° for the validation and approx. 124.4° and 234.9° for the sweep.

TABLE II

Parameter	**Value**
MMI width	14.6 [um]
MMI length	234.9 [um]
Taper width	4.056 [um]
Taper length	15 [um]
Taper m	2
Taper location	0, $\pm 5.146[um]$
S-bend length	132.017 [um]

A phase reconstruction diagram can be seen in figure 6. The figure shows that both the blind and referenced calibration systems do show improvements over the non calibrated output. Figures 7 and 8 show this performance in more detail, as well

as with the addition of noise. This noise was simulated in Matlab as white Gaussian noise and placed directly on top of the validation data, before the calibrations. The limit at high SNR for the maximum phase error is shown to be approx. 8.83° without calibration, 0.30° with blind calibration, and 0.13° with referenced calibration. For the average phase error these are approx. 3.97° without calibration, 0.17° with blind calibration and 0.08° with referenced calibration. Noticeable is that for both the average and maximum phase errors, the difference between blind and referenced calibration becomes very small around an SNR of 50 dB. This would mean that for environments with an SNR up to this value, there is no phase benefit to having access to any known θ as reference. The maximum phase error at 50 dB SNR is approx. 1.86° and the average phase error is approx. 0.56°.

Finally, figure 12 shows the Poynting fields and the outputs of the MMI for a single source, and $\theta = 0, \frac{2\pi}{3}, \frac{4\pi}{3}$. Notice how the power is evenly distributed over the output ports when only a single source is used and that there is always a single highest output in the other images, corresponding with θ.

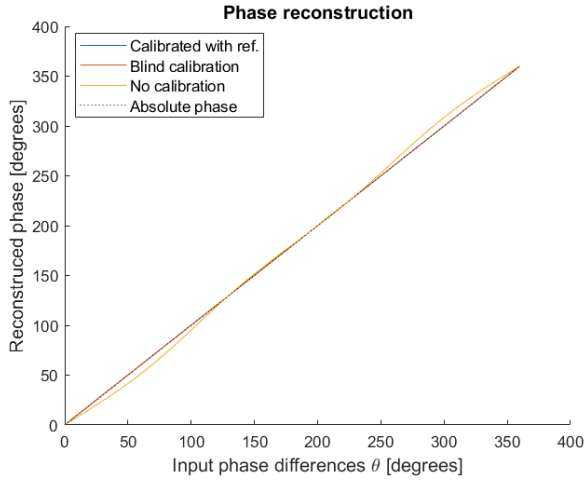

Fig. 6: Phase reconstruction for all three calibration schemes

VII. Conclusion

This report has shown that it is possible to automatically design an 3x3 MMI based downconverter. Although there is some deviation between the estimated and validated devices, this is likely a good trade-off against the efficiency of the program compared to manual design. With blind calibration, which is the most likely method, the average error in determining θ can be shown to be as low as 0.17°.

Being able to investigate a large range of dimensional points also has the benefit of increasing the probability of finding the global maximum instead of a local maximum for the performance of the MMI. The significantly higher simulation speed should allow for rapid prototyping and an interesting prospect, which lay outside the scope of this report, might be to manually fine-tune any generated MMI's to possibly reach even better results.

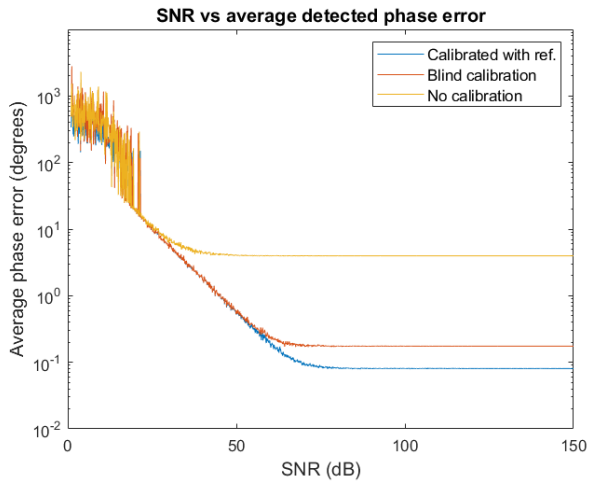

Fig. 7: SNR performance of optimal MMI. Showing the average phase error for all three calibration schemes.

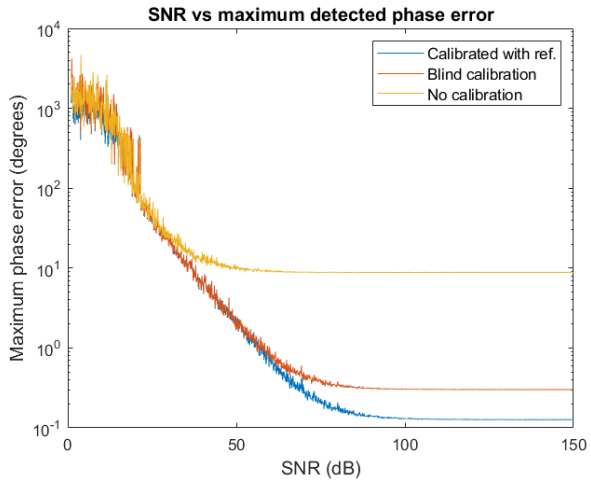

Fig. 8: SNR performance of optimal MMI. Showing the maximum phase error for all three calibration schemes.

Acknowledgements

Writing this paper has turned out to be quite the journey, of course being not only the creation of the automated MMI design, but also the learning process to get up to this point and the many hurdles that had to be overcome with it. I have thoroughly enjoyed the last months and I would like to express my deepest gratitude to Prof. Dr. García Blanco, who has made this thesis possible and especially to my day-to-day supervisor Ward Hendriks MSc whom has continuously pointed me in the right direction and kept me stimulated and motivated the whole time. Many thanks also go out to prof. dr. Pepijn Pinkse as the closing member of the thesis committee. Finally, I would be remiss in not mentioning my girlfriend Femke Meulemans whose love and support have kept me going all this time.

REFERENCES

[1] T. Chalyan, R. Guider, L. Pasquardini, M. Zanetti, F. Falke, E. Schreuder, R. G. Heideman, C. Pederzolli, and L. Pavesi, "Asymmetric mach–zehnder interferometer based biosensors for aflatoxin m1 detection," *Biosensors*, vol. 6, no. 1, 2016. [Online]. Available: https://www.mdpi.com/2079-6374/6/1/1

[2] B. Stern, K. Kim, H. Gariah, and D. Bitauld, "Athermal silicon photonic wavemeter for broadband and high-accuracy wavelength measurements," *Opt. Express*, vol. 29, no. 19, pp. 29 946–29 959, Sep 2021. [Online]. Available: http://opg.optica.org/oe/abstract.cfm?URI=oe-29-19-29946

[3] T. Kawanishi, K. Kogo, S. Oikawa, and M. Izutsu, "Direct measurement of chirp parameters of high-speed mach–zehnder-type optical modulators," *Optics Communications*, vol. 195, no. 5, pp. 399–404, 2001. [Online]. Available: https://www.sciencedirect.com/science/article/pii/S0030401801013529

[4] C. Taballione, R. Meer, H. Snijders, P. Hooijschuur, J. Epping, M. Goede, B. Kassenberg, P. Venderbosch, C. Toebes, H. Vlekkert, P. Pinkse, and J. Renema, "A universal fully reconfigurable 12-mode quantum photonic processor," *Materials for Quantum Technology*, vol. 1, p. 035002, 09 2021.

[5] R. Hui and M. O'Sullivan, *Basic Instrumentation for Optical Measurement*, 12 2009, pp. 129–258.

[6] P. J. Reyes-Iglesias, A. O.-M. nux, and I. Molina-Fernández, "Colorless monolithically integrated 120° downconverter," *Opt. Express*, vol. 21, no. 20, pp. 23 048–23 057, Oct 2013. [Online]. Available: http://opg.optica.org/oe/abstract.cfm?URI=oe-21-20-23048

[7] R. Halir, L. Vivien, X. Le Roux, D.-X. Xu, and P. Cheben, "Direct and sensitive phase readout for integrated waveguide sensors," *IEEE Photonics Journal*, vol. 5, no. 4, pp. 6 800 906–6 800 906, 2013.

[8] P. J. Reyes-Iglesias, I. Molina-Fernández, A. Moscoso-Mártir, and A. O.-M. nux, "High-performance monolithically integrated 120° downconverter with relaxed hardware constraints," *Opt. Express*, vol. 20, no. 5, pp. 5725–5741, Feb 2012. [Online]. Available: http://opg.optica.org/oe/abstract.cfm?URI=oe-20-5-5725

[9] C. M. Lalau-Keraly, S. Bhargava, O. D. Miller, and E. Yablonovitch, "Adjoint shape optimization applied to electromagnetic design," *Opt. Express*, vol. 21, no. 18, pp. 21 693–21 701, Sep 2013. [Online]. Available: http://opg.optica.org/oe/abstract.cfm?URI=oe-21-18-21693

[10] A. W. Snyder and J. Love, *Optical Waveguide Theory*, 1st ed. Springer, 1983. [Online]. Available: https://link.springer.com/book/10.1007/978-1-4613-2813-1

[11] Lumerical-Inc., "Curved waveguide taper (varfdtd and fdtd)." [Online]. Available: https://optics.ansys.com/hc/en-us/articles/360042799713-Curved-waveguide-taper-varFDTD-and-FDTD-

[12] ——, "Tips for creating waveguide bends using the path object." [Online]. Available: https://optics.ansys.com/hc/en-us/articles/360034901673-Tips-for-creating-waveguide-bends-using-the-path-object

[13] P. Besse, M. Bachmann, H. Melchior, L. Soldano, and M. Smit, "Optical bandwidth and fabrication tolerances of multimode interference couplers," *Journal of Lightwave Technology*, vol. 12, no. 6, pp. 1004–1009, 1994.

[14] E. D. Palik and E. J. Prucha, *Handbook of optical constants of solids*. Boston, MA: Academic Press, 1997. [Online]. Available: https://cds.cern.ch/record/396087

[15] M. Bachmann, P. A. Besse, and H. Melchior, "General self-imaging properties in n × n multimode interference couplers including phase relations," *Appl. Opt.*, vol. 33, no. 18, pp. 3905–3911, Jun 1994. [Online]. Available: http://opg.optica.org/ao/abstract.cfm?URI=ao-33-18-3905

[16] K. Cooney and F. H. Peters, "Analysis of multimode interferometers," *Opt. Express*, vol. 24, no. 20, pp. 22 481–22 515, Oct 2016. [Online]. Available: http://opg.optica.org/oe/abstract.cfm?URI=oe-24-20-22481

APPENDIX

A. *Result figures*

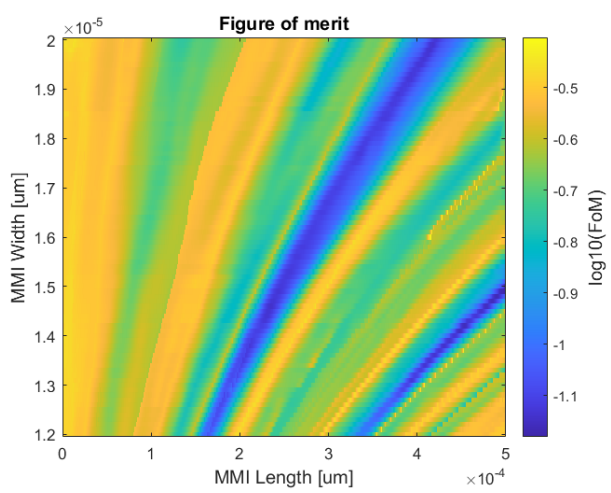

(a) FoM *without* the probability distribution

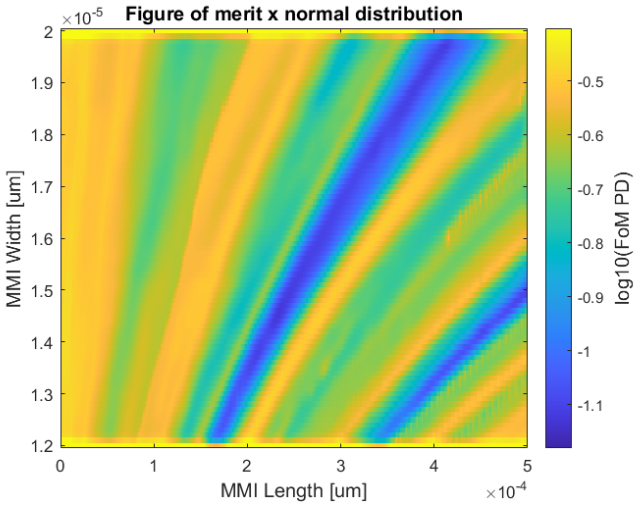

(b) FoM *with* the probability distribution

Fig. 9: Figure of merit results

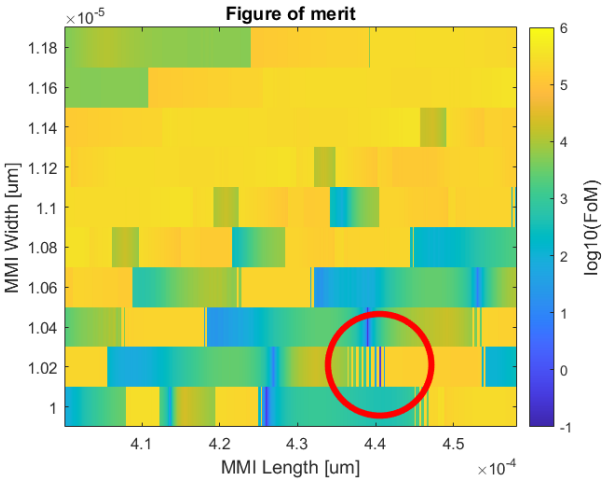

(a) FoM

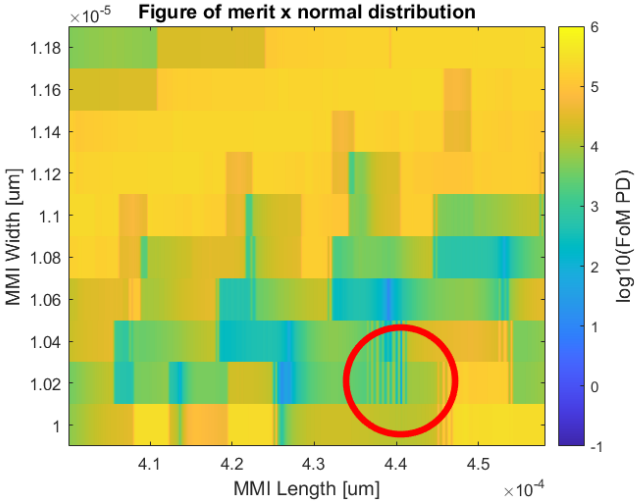

(b) FoM with the probability distribution

Fig. 10: Figure of merit results zoomed around unstable point

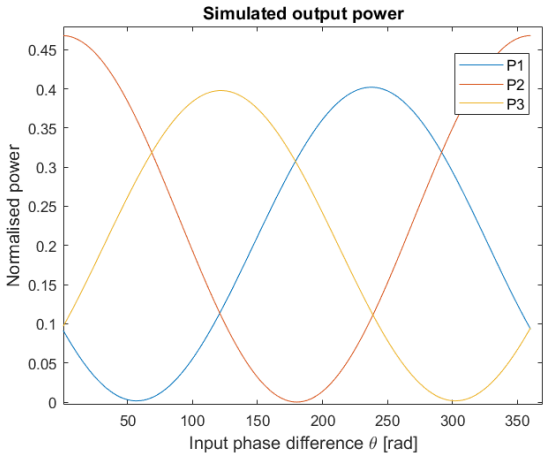

(a) Created by varFDTD simulation

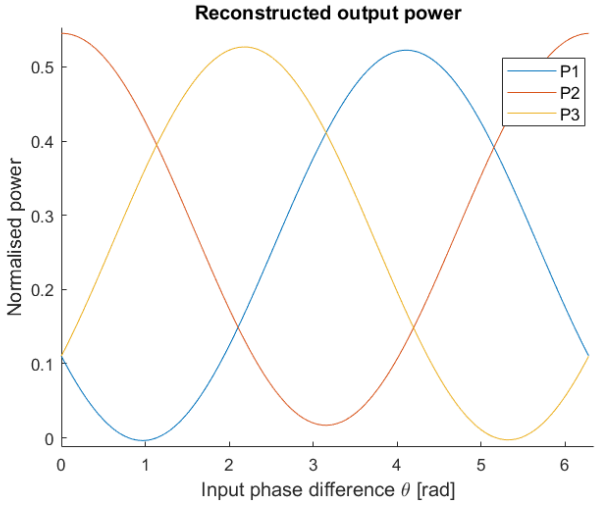

(b) Reconstructed from dimension sweep

Fig. 11: Output power versus input phase difference

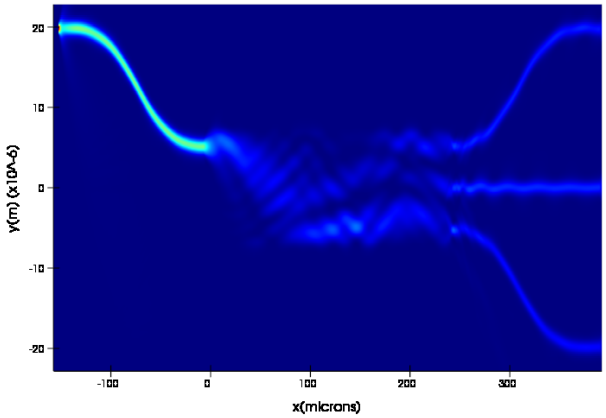

(a) Single source

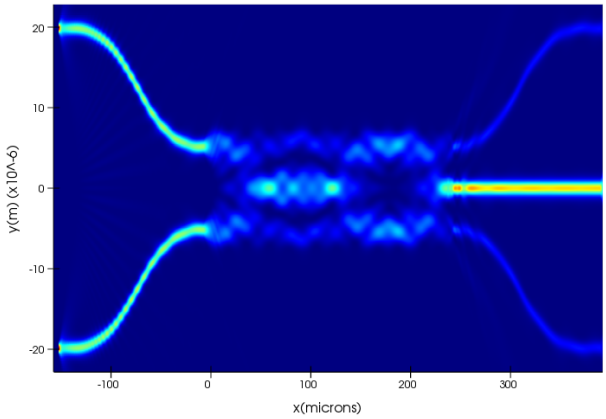

(b) 0° phase difference

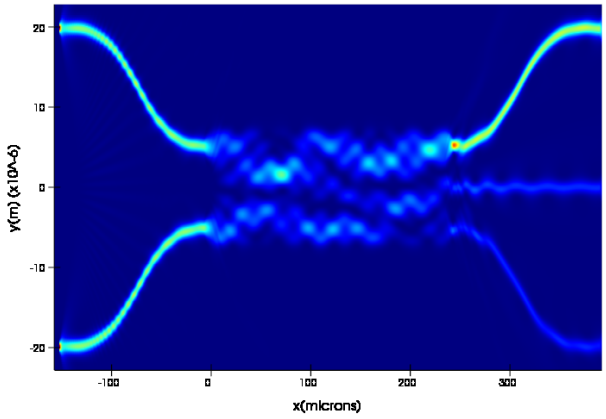

(c) 120° phase difference

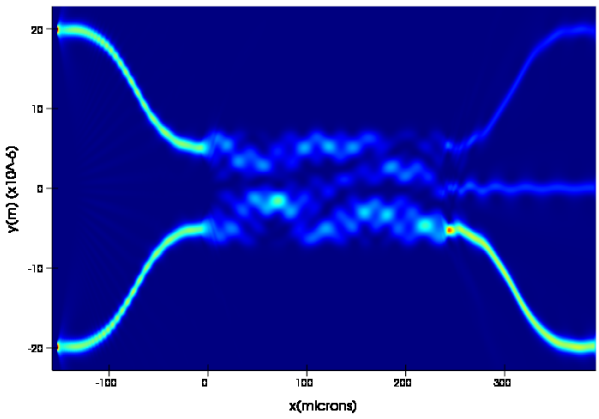

(d) 240° phase difference

Fig. 12: Poynting fields in the MMI with different input phase differences

B. Program overview and code

https://gitlab.utwente.nl/optical-sciences/automated-3x3-mmi

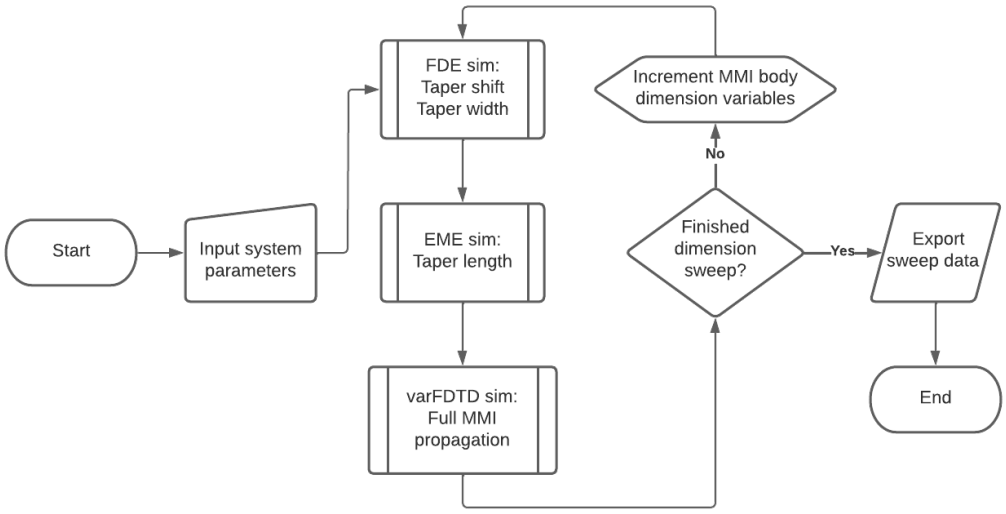

Fig. 13: A flow diagram of the automation program

C. Derivation equation 16: "c" parameter

The derivation for equation 16 starts with the following cosine property:

$$\cos(x) + \cos(x - \frac{2\pi}{3}) + \cos(x - \frac{4\pi}{3}) = 0 \tag{13}$$

Now, using equation 7:

$$\begin{aligned} P_i(0) + P_i(\frac{2\pi}{3}) + P_i(\frac{4\pi}{3}) &= A_i\cos(\theta) + c_i + A_i\cos(\theta - \frac{2\pi}{3}) + c_i + A_i\cos(\theta - \frac{4\pi}{3}) + c_i \\ &= A_i(\cos(\theta) + \cos(\theta - \frac{2\pi}{3}) + \cos(\theta - \frac{4\pi}{3})) + 3c_i \end{aligned} \tag{14}$$

Combining this with the property in equation 13 gives:

$$P_i(0) + P_i(\frac{2\pi}{3}) + P_i(\frac{4\pi}{3}) = A_i \cdot 0 + 3c_i \tag{15}$$

From this directly follows that:

$$c_i = \frac{P_i(0) + P_i(\frac{2\pi}{3}) + P_i(\frac{4\pi}{3})}{3} \tag{16}$$

D. Derivation equation 4: "ϕ" parameter

Using Euler's formula and equation 7:

$$P_i(\theta) = \frac{A_i}{2}(e^{j\theta} \cdot e^{-j\phi} + e^{-j\theta} \cdot e^{j\phi}) + c_i \tag{17}$$

Now, assume:

$$\Delta P_i = \frac{P_i(\frac{2\pi}{3}) - c_i}{P_i(0) - c_i} \tag{18}$$

Combining the above equations gives:

$$\begin{aligned}\Delta P_i &= \frac{\frac{A}{2} \cdot (e^{j\frac{2/pi}{3}} \cdot e^{-j\phi} + e^{-j\frac{2/pi}{3}} \cdot e^{j\phi})}{\frac{A}{2} \cdot (e^{j\cdot 0} \cdot e^{-j\phi} + e^{-j\cdot 0} \cdot e^{j\phi})} \\ &= \frac{e^{j\frac{2/pi}{3}} \cdot e^{-j\phi} + e^{-j\frac{2/pi}{3}} \cdot e^{j\phi}}{e^{-j\phi} + e^{j\phi}}\end{aligned} \tag{19}$$

For ease of notation, let's say $e^{j\phi} = x$ and $e^{j\frac{2\pi}{3}} = y$, then continuing with the above equations gives:

$$\begin{aligned}\Delta P_i &= \frac{x^{-1} \cdot y + x \cdot y^{-1}}{x^{-1} + x} \\ \Delta P_i &= \frac{y + x^2 \cdot y^{-1}}{1 + x^2} \\ \Delta P_i \cdot (1 + x^2) &= y + x^2 \cdot y^{-1} \\ \Delta P_i + \Delta P_i \cdot x^2 &= y + x^2 \cdot y^{-1} \\ x^2 \cdot y^{-1} - \Delta P_i \cdot x^2 &= \Delta P_i - y \\ x^2(y^{-1} - \Delta P_i) &= \Delta P_i - y \\ x^2 &= \frac{\Delta P_i - y}{y^{-1} - \Delta P_i} \\ x &= \pm\sqrt{\frac{\Delta P_i - y}{y^{-1} - \Delta P_i}}\end{aligned} \tag{20}$$

Which, by re-substituting the values for x and y, and assuming x to be positive, results in:

$$e^{j\phi_i} = \frac{\sqrt{\Delta P_i - e^{j\frac{2\pi}{3}}}}{\sqrt{e^{-j\frac{2\pi}{3}} - \Delta P_i}} \tag{21}$$

E. Derivation of equation 6: "A" parameter

From equation 7:

$$P_i(0) = A\cos(-\phi) + c \tag{22}$$

Using the cosine property $\cos(x) = \cos(-x)$ gives:

$$P_i(0) = A_i\cos(\phi) + c_i \tag{23}$$

From which directly follows:

$$A_i = \frac{(P_i(0) - c_i)}{\cos(\phi_i)} \tag{24}$$